



1 **Long-term trends of ambient nitrate (NO<sub>3</sub><sup>-</sup>) concentrations across China based on ensemble**  
2 **machine-learning models**

3 Rui Li<sup>a</sup>, Lulu Cui<sup>a\*</sup>, Yilong Zhao<sup>a</sup>, Wenhui Zhou<sup>a</sup>, Hongbo Fu<sup>a,b,c\*</sup>

4 <sup>a</sup> *Shanghai Key Laboratory of Atmospheric Particle Pollution and Prevention, Department of*  
5 *Environmental Science & Engineering, Institute of Atmospheric Sciences, Fudan University,*  
6 *Shanghai, 200433, P.R. China*

7 <sup>b</sup> *Collaborative Innovation Center of Atmospheric Environment and Equipment Technology*  
8 *(CICAET), Nanjing University of Information Science and Technology, Nanjing 210044, P.R.*  
9 *China*

10 <sup>c</sup> *Shanghai Institute of Pollution Control and Ecological Security, Shanghai 200092, P.R. China*

11 **\* Correspondence to:**

12 Drs. H. Fu (Email: [fuhb@fudan.edu.cn](mailto:fuhb@fudan.edu.cn)) and L. Cui (Email: [15110740004@fudan.edu.cn](mailto:15110740004@fudan.edu.cn))

13 **Abstract**

14 High loadings of nitrate (NO<sub>3</sub><sup>-</sup>) in the aerosol over China significantly exacerbates the air quality  
15 and poses a great threaten on ecosystem safety through dry/wet deposition. Unfortunately, limited  
16 ground-level observation data makes it challenging to fully reflect the spatial pattern of NO<sub>3</sub><sup>-</sup> level  
17 across China. Up to date, the long-term monthly NO<sub>3</sub><sup>-</sup> datasets at a high resolution were still missing,  
18 which restricted the assessment of human health and ecosystem safety. Therefore, a unique monthly  
19 NO<sub>3</sub><sup>-</sup> dataset at 0.25 ° resolution over China during 2005-2015 was developed by assimilating  
20 surface observation, satellite product, meteorological data, land use types and other covariates using  
21 an ensemble model combining random forest (RF), gradient boosting decision tree (GBDT), and  
22 extreme gradient boosting (XGBoost). The new developed product featured excellent cross-  
23 validation R<sup>2</sup> value (0.78) and relatively lower root-mean-square error (RMSE: 1.19 µg/m<sup>3</sup>) and  
24 mean absolute error (MAE: 0.81 µg/m<sup>3</sup>). Besides, the dataset also exhibited relatively robust



25 performance at the spatial and temporal scale. Moreover, the dataset displayed good agreement with  
26 ( $R^2 = 0.85$ ,  $RMSE = 0.74 \mu\text{g}/\text{m}^3$ , and  $MAE = 0.55 \mu\text{g}/\text{m}^3$ ) some unlearning data collected from  
27 previous studies. The spatiotemporal variations of the developed product were also shown. The  
28 estimated  $\text{NO}_3^-$  concentration showed the highest value in North China Plain (NCP) ( $3.55 \pm 1.25$   
29  $\mu\text{g}/\text{m}^3$ ), followed by Yangtze River Delta (YRD ( $2.56 \pm 1.12 \mu\text{g}/\text{m}^3$ )), Pearl River Delta (PRD ( $1.68$   
30  $\pm 0.81 \mu\text{g}/\text{m}^3$ )), Sichuan Basin ( $1.53 \pm 0.63 \mu\text{g}/\text{m}^3$ ), and the lowest one in Tibetan Plateau ( $0.42 \pm$   
31  $0.25 \mu\text{g}/\text{m}^3$ ). The higher ambient  $\text{NO}_3^-$  concentrations in NCP, YRD, and PRD were closely linked  
32 to the dense anthropogenic emissions. Apart from the intensive human activities, poor terrain  
33 condition might be a key factor for the serious  $\text{NO}_3^-$  pollution in Sichuan Basin. The lowest ambient  
34  $\text{NO}_3^-$  concentration in Tibetan Plateau was contributed by the scarce anthropogenic emission and  
35 favorable meteorological factors (e.g., high wind speed). In addition, the ambient  $\text{NO}_3^-$   
36 concentration showed marked increasing tendency of  $0.10 \mu\text{g}/\text{m}^3/\text{year}$  during 2005-2014 ( $p < 0.05$ ),  
37 while it decreased sharply from 2014 to 2015 at a speed of  $-0.40 \mu\text{g}/\text{m}^3/\text{year}$  ( $p < 0.05$ ). The ambient  
38  $\text{NO}_3^-$  levels in Beijing-Tianjin-Hebei (BTH), YRD, and PRD displayed gradual increases at the  
39 speed of 0.13, 0.08, and  $0.03 \mu\text{g}/\text{m}^3/\text{year}$  ( $p < 0.05$ ) during 2005-2014, respectively. The gradual  
40 increases of  $\text{NO}_3^-$  concentrations in these regions from 2005 to 2014 were due to that the emission  
41 reduction measures during this period focused on the reduction of  $\text{SO}_2$  emission rather than  $\text{NO}_x$   
42 emission and the rapid increase of energy consumption. Afterwards, the government further  
43 strengthened these emission reduction measures, and thus caused the dramatic decreases of  $\text{NO}_3^-$   
44 concentrations in these regions from 2014 to 2015 ( $p < 0.05$ ). The long-term  $\text{NO}_3^-$  dataset over  
45 China could greatly deepen the knowledge about the impacts of emission reduction measures on air



46 quality improvement. The monthly particulate  $\text{NO}_3^-$  levels over China during 2005-2015 are open  
47 access in <https://doi.org/10.5281/zenodo.3988307> (Li et al., 2020c).

## 48 **1. Introduction**

49 Reactive nitrogen ( $\text{N}_r$ ) emissions displayed remarkable increases in the past decades owing to  
50 the high-speed industrial development and urbanization (Cui et al., 2016; Singh et al., 2017).  
51 Ambient reactive N emissions were mainly characterized with nitrogen oxides ( $\text{NO}_x$ ), accounting  
52 for about 30% of the gross  $\text{N}_r$  emissions (Chen et al., 2015; Liu et al., 2011). These important N-  
53 bearing precursors could be transformed into the nitrate ( $\text{NO}_3^-$ ) via multiple chemical pathways (e.g.,  
54 heterogeneous or liquid phase reaction), and finally deposited in the terrestrial or aquatic ecosystem  
55 (Jia et al., 2016; Qiao et al., 2015; Zhao et al., 2017). On the one hand, heavy loadings of  $\text{NO}_3^-$   
56 greatly degraded the atmospheric visibility and cool the surface of the Earth system because  
57 particulate  $\text{NO}_3^-$  significantly scattered solar radiation (Fu and Chen, 2017). Moreover, enhanced N  
58 deposition might pose a negative effect on the ecosystem health such as biodiversity losses,  
59 freshwater eutrophication, and oceanic acidification (Compton et al., 2011; Erisman et al., 2013).  
60 Hence, deepening the knowledge about the spatial patterns and long-term trends of particulate  $\text{NO}_3^-$   
61 in the atmosphere is beneficial to accurately evaluate the ecological and environmental effects of N  
62 deposition.

63 Ground-level observation is often acknowledged to be an effective means to explore the spatial  
64 patterns of ambient  $\text{NO}_3^-$  concentrations. Many long-term monitoring networks including Clean Air  
65 Status and Trends Network (CASTNET) and Canadian Air and Precipitation Monitoring Network  
66 (CAPMoN) were established to quantify the ambient  $\text{NO}_3^-$  concentration and inorganic N deposition.  
67 Du et al. (2014) revealed that the  $\text{NO}_3^-$  deposition showed significant decrease across the United



68 States during 1985-2012 based on these observation data. To date, most of these observation  
69 networks focused on North America and Europe, whereas few monitoring sites were located on East  
70 Asia especially on China. Fortunately, China has constructed some ground-level observation  
71 networks such as CARE-China Observation Network in recent years. On the basis of these  
72 observation networks, the overall spatiotemporal trend of particulate  $\text{NO}_3^-$  concentration has been  
73 clarified (Wang et al., 2019c; Xu et al., 2018a). Xu et al. (2018a) observed that the particulate  $\text{NO}_3^-$   
74 concentration ( $< 4.5 \mu\text{m}$ ) over China did not show significantly temporal variation during 2011-  
75 2015. Very recently, Wang et al. (2019) found that the  $\text{NO}_3^-$  level in the fine particle ( $\text{PM}_{2.5}$ )  
76 decreased by 34% during 2015-2017. Although the overall spatial patterns have been preliminarily  
77 revealed based on these isolated sites, these sparse ground-observed sites might not reflect the high-  
78 resolution  $\text{NO}_3^-$  pollution across China because each station only possessed limited spatial  
79 representative and  $\text{NO}_3^-$  concentration was often highly variable in space and time (Liu et al., 2017a).  
80 More importantly, the current studies only investigated the ambient  $\text{NO}_3^-$  concentrations in recent  
81 years, while the long-term variation of  $\text{NO}_3^-$  level remained unknown. It was well known that the  
82 energy consumption in China displayed remarkable increase in recent decades (Zhan et al., 2018).  
83 Meanwhile, Chinese government also proposed pollutant emission reduction policies since 2005 to  
84 ensure the coordinated development of economic growth and environmental protection (Ma et al.,  
85 2019). However, the synergistic effects of air pollution control policies and increased energy  
86 consumption on long-term evolution trend of  $\text{NO}_3^-$  pollution over China were not assessed yet,  
87 which were extremely critical for the implementation of emission control measures.

88 To complement the gaps of ground-level observations, satellite product of  $\text{NO}_2$  is regarded as a  
89 welcome addition to investigate the long-term trends of N-bearing components in the atmosphere.



90 Ozone Monitoring Instrument (OMI) was regarded as the typical satellite product applied to  
91 simulate the ambient  $\text{NO}_3^-$  concentration (Liu et al., 2017b; Vrekoussis et al., 2013). Jia et al. (2016)  
92 firstly used the linear regression method to predict the  $\text{NO}_3^-$  levels and dry deposition fluxes at the  
93 global scale based on OMI-derived  $\text{NO}_2$  column amount. However, the dry deposition fluxes of  
94  $\text{NO}_3^-$  modelled by Jia et al. (2016) showed weak correlation with the measured value ( $R = 0.47$ ),  
95 which might be attributable to the simple linear assumption between  $\text{NO}_2$  column amount and  $\text{NO}_3^-$   
96 deposition flux. It was well documented that the nonlinearity relationship between multiple  
97 predictors and  $\text{NO}_3^-$  concentration were hard to reveal on the basis of the simple linear model (Zhan  
98 et al., 2018a; Zhan et al., 2018b). To enhance the predictive performance of  $\text{NO}_3^-$  concentration, Liu  
99 et al. (2017) used the chemical transport models (CTMs) to estimate the dry deposition fluxes of N-  
100 bearing species recently based on the remotely sensed  $\text{NO}_2$  column amount. However, CTMs often  
101 suffered from high uncertainty because of the limited knowledge about the generation pathways for  
102 particulate  $\text{NO}_3^-$  in the atmosphere (Zhan et al., 2018a). Recently, the emergence of machine  
103 learning models provided unprecedented opportunities to estimate the concentrations of N-bearing  
104 components (Chen et al., 2019b; Zhan et al., 2018b). It was well known that the machine learning  
105 models generally showed the better predictive accuracy than CTMs and traditional statistical models  
106 when the training samples were sufficient (Zang et al., 2019; Zhan et al., 2017). In the pioneering  
107 studies, the  $\text{NO}_2$  estimation has aroused widespread concern (Zhan et al., 2018b; Chen et al., 2019).  
108 Zhan et al. (2018b) employed random forest (RF) coupled with spatiotemporal Kriging model to  
109 simulate the ambient  $\text{NO}_2$  levels over China, and achieved the moderate modelling performance ( $R^2$   
110 = 0.62). Afterwards, Chen et al. (2019) used the extreme gradient boosting (XGBoost) model  
111 combined with kriging-calibrated satellite method to estimate the national  $\text{NO}_2$  concentration and



112 significantly improved the predictive performance ( $R^2 = 0.85$ ). Up to date, no study utilized the  
113 machine-learning models to significantly improve the predictive accuracy of  $\text{NO}_3^-$  concentration.  
114 Moreover, nearly all of the current studies only focused on the spatial pattern of particulate  $\text{NO}_3^-$   
115 level in China (Liu et al., 2017; Jia et al., 2016), while they cannot establish a long-term  $\text{NO}_3^-$  dataset  
116 across China.

117 Here, we firstly developed a high-resolution ( $0.25^\circ$ ) monthly  $\text{NO}_3^-$  dataset across China during  
118 2005-2015 based an ensemble model including RF, XGBoost, and gradient boosting decision tree  
119 (GBDT) algorithms. At first, the modelling performance and improvement of this new-developed  
120 product compared with previous datasets were evaluated. Afterwards, we analyzed the spatial  
121 variation and long-term evolution trend of estimated  $\text{NO}_3^-$  concentration over China and explored  
122 the potential impacts of air pollution control measures on  $\text{NO}_3^-$  variation. The long-term  $\text{NO}_3^-$   
123 datasets could supply scientific judge for policy makers to mitigate the severe nitrate pollution in  
124 China.

## 125 **2. Input data**

### 126 **2.1 Ground-level $\text{NO}_3^-$ data**

127 The monthly  $\text{NO}_3^-$  monitoring data during 2010-2015 were collected from NNDMN including  
128 32 sites (Fig. 1 and Fig. S1), and these sites could be divided into three types including urban, rural,  
129 and background sites (Xu et al., 2018a). Ambient concentrations of particulate  $\text{NO}_3^-$  were  
130 determined on the basis of an active DELTA (DENuder for Long-Term Atmospheric sampling)  
131 system. The system comprises of a pump, a filter sampling instrument, and a dry gas meter with  
132 high sensitivity. Two set of filters in a 2-stage filter pack was applied to sample the aerosol particles,  
133 with a first  $\text{K}_2\text{CO}_3$ /glycerol impregnated filter to obtain  $\text{NO}_3^-$  particles. All of the monitoring sites



134 kept the same sampling frequency at the month scale. The detailed sampling and analysis procedures  
135 have been described by Xu et al. (2018). The detection limit of particulate  $\text{NO}_3^-$  concentration over  
136 China is  $0.05 \mu\text{g}/\text{m}^3$ .

### 137 2.2 Satellite product of $\text{NO}_2$ column density

138 The OMI- $\text{NO}_2$  level-3 tropospheric column densities ( $0.25^\circ$  resolution) were used to predict the  
139  $\text{NO}_3^-$  concentration (Fig. S2). The OMI aboard on the Aura satellite was available since September,  
140 2004, which displayed global coverage and crossed the entire earth each day. OMI possessed three  
141 spectral channels ranging from 270 to 500 nm, and thus was often applied to monitor the gaseous  
142 pollutants such as  $\text{NO}_2$ ,  $\text{SO}_2$ , and  $\text{O}_3$ .

143 In this study, we downloaded the daily  $\text{NO}_2$  columns during 2005-2015 from  
144 <https://earthdata.nasa.gov/>. The tropospheric  $\text{NO}_2$  column density data of poor quality (e.g., cloud  
145 radiance fraction  $> 0.5$ , solar zenith angles  $> 85^\circ$ , and terrain reflectivity  $> 30\%$ ) should be removed.  
146 Additionally, the cross-track pixels sensitive to significant row anomaly also must be deleted.  
147 Finally, the monthly  $\text{NO}_2$  columns were estimated by averaging the daily  $\text{NO}_2$  columns.

### 148 2.3 Meteorological factors, land use types, and other variables

149 These independent variables for particulate  $\text{NO}_3^-$  estimates were gained from multiple sources.  
150 The meteorological data on a daily basis were downloaded from ERA-Interim datasets ( $0.25^\circ$   
151 resolution) in the website of <http://www.ecmwf.int/> (Table S1). Among all of the daily  
152 meteorological data in ECMWF website, 2-m temperature ( $T_{2m}$ ), 2-m dewpoint temperature ( $D_{2m}$ ),  
153 10-m U wind component ( $U_{10}$ ), 10-m V wind component ( $V_{10}$ ), sunshine duration (Sund), surface  
154 pressure (Sp), boundary layer height (BLH), and total precipitation (Tp). The elevation, gross  
155 domestic production (GDP), and population density (PD) data over China were downloaded from



156 the website of <http://www.resdc.cn/>. PD and GDP in 1995, 2000, 2005, 2010, and 2015 were linearly  
157 interpolated to calculate PD and GDP in each year. Afterwards, these data were incorporated into  
158 the final model to predict the particulate  $\text{NO}_3^-$  concentration over China. In addition, the land use  
159 data (e.g., grassland, forest, urban, and agricultural land) were also downloaded from the website of  
160 <http://www.resdc.cn/>.

161 These independent variables collected from various sources were uniformly resampled to  $0.25^\circ$   
162  $\times 0.25^\circ$  grids. For instance, the land use area, GDP, and PD in  $0.25^\circ$  grid was calculated based on  
163 area-weighted average algorithm. To ensure the better predictive performance, it was necessary to  
164 employ the appropriate variable selection method to remove some redundant predictors. The basic  
165 principle of the variable choice was to remove the variables with the lower importance values. The  
166 variables could be regarded as the redundant ones when the  $R^2$  value of the final model showed  
167 dramatic decrease after removing them.

### 168 3. Methods

#### 169 3.1 Ensemble model development

170 In the previous studies concerning about air pollution prediction, RF, gradient boosting decision  
171 tree (GBDT), and extreme gradient boosting (XGBoost) showed good predictive performance (Li  
172 et al., 2020a). RF model possesses a large amount of decision trees, and each one suffered from an  
173 independent sampling process and these trees displayed the same distribution (Breiman, 2001). This  
174 model generally shows the higher prediction accuracy due to the injected randomness. The model  
175 performance mainly relies on the number of trees, the variable group, and the splitting features. The  
176 detailed algorithms are shown as follows:

$$177 \quad f(x) = \sum_{z=1}^Z c_z I(x \in M_z) \quad (1)$$





178 
$$\hat{c}_z = \text{mean}(y_i | x_i \in M_z) \quad (2)$$

179 
$$L_1(m, n) = \{X | X_j \leq n\} \& L_2(m, n) = \{X | X_j > n\} \quad (3)$$

180 
$$\min_{m,n} \left[ \min_{M_1(m,n)} \sum (y - c_1)^2 + \min_{M_2(m,n)} \sum (y - c_2)^2 \right] \quad (4)$$

181 
$$\hat{c}_1 = \text{mean}(y_i | x_i \in M_1(m, n)) \& \hat{c}_2 = \text{mean}(y_i | x_i \in M_2(m, n)) \quad (5)$$

182 where  $(x_i, y_i)$  denotes the sample for  $i = 1, 2, \dots, N$  in  $M$  regions ( $M_1, M_2, \dots, M_z$ ),  $c_m$  represents  
 183 the response to the model,  $\hat{c}_z$  denotes the best value,  $m$  represents the feature variable, and  $n$  is  
 184 the split point.

185 GBDT model is often considered to be a typical boosting method. Compared with RF model,  
 186 each classifier is applied to decrease the residual of the last round. The detailed equations are as  
 187 follows:

188 
$$c_{ij} = \arg \min_{x_i \in R_{ij}} \sum L(y_i, f_{i-1}(x_i) + c) \quad (6)$$

189 
$$f_i(x) = f_{i-1}(x) + \sum_{j=1}^J c_{ij} I \quad (7)$$

190  $c_{ij}$  denotes the predicted the estimation error in the last round;  $y_i$  represents the observed value;  
 191  $f_{i-1}(x_i)$  is the predicted value in the last round.  $c$  was regarded as the optimal value when  $c_{ij}$  reaches  
 192 the least value.

193 XGBoost method is an updated version of GBDT model and loss functions are expanded to the  
 194 second order function. On the basis of the pioneering studies (Chen et al., 2019a), XGBoost  
 195 generally shows excellent performance because of its high efficiency and impressive accuracy. The  
 196 detailed XGBoost algorithm is shown as the following formula (Zhai and Chen, 2018):

197 
$$L^{(t)} = \sum_{i=1}^n [l(y_i, y^{\Lambda(t-1)}) + \partial_{y^{\Lambda(t-1)}} l(y_i, y^{\Lambda(t-1)}) f_i(x_i) + \frac{1}{2} \partial_{y^{\Lambda(t-1)}}^2 l(y_i, y^{\Lambda(t-1)}) f_i^2(x_i)] + \Omega(f_i) \quad (8)$$



198 where  $L^{(t)}$  represents the cost function at the  $t$ -th period.  $l$  is the differentiable convex loss function  
199 that reveals the difference of the predicted value ( $\hat{y}$ ) of the  $i$ -th instance at the  $t$ -th period and the  
200 target value ( $y_i$ ).  $f_i(x)$  denotes the increment.

201 However, each model still shows some disadvantages in the prediction accuracy. Consequently,  
202 it was proposed to combine these models with multiple linear regression (MLR) model to further  
203 estimate monthly  $\text{NO}_3^-$  concentration in the atmosphere over China. As shown in Fig. 2, three  
204 submodels including RF, GBDT, and XGBoost were stacked through MLR model to estimate the  
205 monthly  $\text{NO}_3^-$  concentration over China. At first, a 5-fold cross-validation method was adopted to  
206 train each submodel to determine the appropriate parameter. Afterwards, the MLR model was  
207 trained with the final simulated concentrations of three submodels and observations. Finally, the  
208 high-resolution ambient  $\text{NO}_3^-$  level over China were estimated based on the optimal ensemble model.  
209 The detailed algorithms are shown as follows (Fig. 2):

$$210 \quad \text{NO}_3^- = A \times \text{Pred\_RF} + B \times \text{Pred\_GBDT} + C \times \text{Pred\_XGBoost} + e_{ij} \quad (9)$$

211 where  $\text{Pred\_RF}$ ,  $\text{Pred\_GBDT}$ , and  $\text{Pred\_XGBoost}$  denote the predicted  $\text{NO}_3^-$  concentrations by RF,  
212 GBDT, and XGBoost, respectively.  $A$ ,  $B$ , and  $C$  represent the partial regression coefficients of RF,  
213 GBDT, and XGBoost predictors, respectively.

214 The RF model was trained using matlab2019a with a package named random forest-master. Both  
215 of GBDT and XGBoost algorithms were conducted using many packages named *gbm*, *caret*, and  
216 *xgboost* in R software.

### 217 3.2 The error estimation and uncertainty assessment

218 The estimation performance of the ensemble model was evaluated based on 10-fold cross-  
219 validation algorithm. The principle of this method meant that the entire datasets were divided into



220 10 groups with the same capacity randomly. Nine groups were applied to develop the model and the  
221 remained one was used to predict the  $\text{NO}_3^-$  level. After ten rounds, every observed  $\text{NO}_3^-$   
222 concentration showed a corresponding predicted value. Some key indices such as determination  
223 coefficient ( $R^2$ ), root mean square error (RMSE), and mean absolute prediction error (MAE) were  
224 selected as the key indicators to identify the optimal modelling method.

225 The uncertainty of ensemble model were mainly derived from input ancillary variables. For  
226 instance, both of the satellite data and meteorological data often suffered from some uncertainties.  
227 To quantify the uncertainties derived from meteorological data, the meteorological data at  $0.25^\circ$   
228 across China were validated using ground-measured meteorological data downloaded from the  
229 website of Chinese Meteorology Bureau (<http://data.cma.cn/>). Additionally,  $\text{NO}_2$  columns generally  
230 suffered from some uncertainties, whereas the uncertainties of these  $\text{NO}_2$  columns cannot be  
231 determined because the data about the ground-level  $\text{NO}_2$  columns were not open access. In our study,  
232 we only estimated the missing ratio of  $\text{NO}_2$  column, thereby evaluating the uncertainty of  $\text{NO}_3^-$   
233 dataset.

### 234 3.3 Trend analysis

235 The trend analysis of particulate  $\text{NO}_3^-$  concentration was performed using the Mann-Kendall  
236 nonparametric test. This method has been widely applied to analyze the historical trends of carbon  
237 fluxes (Tang et al., 2019) and air quality (Kong et al., 2020), which could reflect whether these data  
238 suffered from significant changes at a significance level of 0.05.

## 239 4. Results and discussion

### 240 4.1 Descriptive statistics of observed $\text{NO}_3^-$ concentrations

241 The ensemble model were applied to fit the  $\text{NO}_3^-$  estimation model based on 1636 matched



242 samples across China during 2010-2015. In general, the site-based  $\text{NO}_3^-$  concentration over China  
243 ranged from  $0.3 \mu\text{g}/\text{m}^3$  in Bayinbrook of Xinjiang province to  $7.1 \mu\text{g}/\text{m}^3$  in Zhengzhou of Henan  
244 province with the mean value of  $2.7 \pm 1.7 \mu\text{g}/\text{m}^3$ . The monthly  $\text{NO}_3^-$  concentrations displayed the  
245 highest and lowest values in North China Plain (NCP) and Tibetan Plateau, respectively. Besides,  
246 the monthly  $\text{NO}_3^-$  level exhibited significantly temporal variation during 2010-2015. The ambient  
247  $\text{NO}_3^-$  concentrations in most of sites displayed the gradual increase during 2010-2014, while they  
248 decreased sharply from 2014 to 2015. The spatiotemporal variation of ambient  $\text{NO}_3^-$  concentration  
249 over China shared similar characteristic with  $\text{NO}_2$  column amount and urban land area (Fig. S2).  
250 The Pearson correlation analysis revealed that the monthly  $\text{NO}_3^-$  level showed the significantly  
251 positive relationship with  $\text{NO}_2$  column amount ( $r = 0.57$ ,  $p < 0.01$ ) and urban land area ( $r = 0.35$ ,  $p$   
252  $< 0.05$ ) (Fig. S3). However,  $D_{2\text{m}}$  showed the remarkably negative correlation with ambient  $\text{NO}_3^-$   
253 concentration ( $r = -0.31$ ,  $p < 0.05$ ).

#### 254 4.2 The validation of new-developed $\text{NO}_3^-$ dataset and comparison with previous products

255 In our study, the ensemble model was applied to develop a monthly  $\text{NO}_3^-$  dataset over China  
256 based on various predictors. Besides, other three individual models were also trained to compare  
257 with their predictive performances. The cross-validation result indicated that the  $R^2$  value of the new  
258 product developed by ensemble decision trees model reached 0.78, significantly higher than those  
259 developed by RF (0.57), GBDT (0.73), and XGBoost (0.45). Nonetheless, both of RMSE and MAE  
260 exhibited the opposite trends. The RMSE value was in the order of XGBoost ( $1.98 \mu\text{g}/\text{m}^3$ ) > RF  
261 ( $1.67 \mu\text{g}/\text{m}^3$ ) > GBDT ( $1.35 \mu\text{g}/\text{m}^3$ ) > ensemble model ( $1.19 \mu\text{g}/\text{m}^3$ ). The MAE value followed the  
262 similar characteristic with the order of XGBoost ( $1.29 \mu\text{g}/\text{m}^3$ ) > RF ( $0.99 \mu\text{g}/\text{m}^3$ ) > GBDT ( $0.95$   
263  $\mu\text{g}/\text{m}^3$ ) > ensemble model ( $0.81 \mu\text{g}/\text{m}^3$ ). Wolpert (1992) suggested the combination of various



264 machine-learning models can significantly strengthen the transferability of models. Chen et al.  
265 (2019a) demonstrated that the ensemble model significantly outperformed the individual machine-  
266 learning model because the ensemble model can overcome the weaknesses of individual model.  
267 Besides, we also assessed the annual modelling performance of  $\text{NO}_3^-$  estimation. Figure S4 shows  
268 that the  $R^2$  value of annual  $\text{NO}_3^-$  estimation reached 0.81, slightly higher than monthly  $\text{NO}_3^-$   
269 prediction (0.78). Furthermore, both of RMSE ( $1.23 \mu\text{g}/\text{m}^3$ ) and MAE ( $0.85 \mu\text{g}/\text{m}^3$ ) for annual  $\text{NO}_3^-$   
270 estimation were slightly higher than those of monthly  $\text{NO}_3^-$  prediction.

271 The new developed  $\text{NO}_3^-$  dataset showed the markedly temporal discrepancy. The  $R^2$  values of  
272  $\text{NO}_3^-$  estimates during 2011-2015 (0.88, 0.89, 0.83, 0.74, and 0.78) were notably higher than that  
273 during 2010 (0.62) (Table 1 and Fig. 3). The relatively lower  $R^2$  value in 2010 attested to the  
274 dominant role of sampling size on the predictive accuracy for machine-learning models. The training  
275 samples in 2010 (135 samples) were notably less than those in other years due to the lack of  
276 observation data in spring. However, both of RMSE and MAE were not sensitive to the sampling  
277 size. The higher RMSE and MAE focused on the 2010, 2014, and 2015. The higher RMSE and  
278 MAE observed in 2010 might be contributed by the poor predictive performance, while the higher  
279 RMSE and MAE likely attained to the higher  $\text{NO}_3^-$  levels during other years. In addition, the  
280 performance of the  $\text{NO}_3^-$  dataset varied greatly at the seasonal scale. The  $R^2$  value was in the order  
281 of summer (0.85) > spring (0.80) = autumn (0.80) > winter (0.75) across China (Table 2). The  
282 seasonal variation of  $\text{NO}_3^-$  concentration was in contrast to the results of fine particle modelled by  
283 previous studies (Li et al., 2020a; Qin et al., 2018). It was supposed that AOD was sensitive to the  
284 precipitation and relative humidity, and thus showed the worse performance in summer. However,  
285 the predictive accuracy of  $\text{NO}_3^-$  estimation based on  $\text{NO}_2$  column amount was closely linked with



286 the chemical transformation from  $\text{NO}_2$  to  $\text{NO}_3^-$ .

287 The  $\text{NO}_3^-$  dataset also displayed markedly spatial variation. The highest  $R^2$  value was observed  
288 in NCP (0.70), followed by Southwest China (0.60), Southeast China (0.59), Northwest China (0.55),  
289 and the lowest one in Northeast China (0.44) (Table 3). The highest  $R^2$  value occurring in NCP was  
290 mainly attributable to the largest training samples ( $> 400$ ) compared with other regions. Southeast  
291 China and Southwest China showed satisfactory cross-validation  $R^2$  values because the valid  
292 training samples in both of these regions were higher than 300. Although both of Northeast China  
293 and Northwest China possessed limited training samples ( $< 200$ ), the predictive performances of  
294 these regions showed significant discrepancy. It was assumed that the sampling sites in Northeast  
295 China were very centralized, while the sampling sites in Northwest China were uniformly  
296 distributed across the whole region. Geng et al. (2018) revealed that the modelling accuracy based  
297 on statistical models were significantly affected by the distribution characteristics of sampling sites.  
298 However, both of RMSE and MAE showed different spatial distributions with the  $R^2$  value and  
299 slope of fitting curve. Note that the higher values of RMSE and MAE were concentrated on  
300 Southwest China (2.08 and 1.41  $\mu\text{g}/\text{m}^3$ ) and Northwest China (2.06 and 1.38  $\mu\text{g}/\text{m}^3$ ) rather than  
301 NCP (1.74 and 1.06  $\mu\text{g}/\text{m}^3$ ). There are two reasons responsible for the result. At first, the predictive  
302 performances of Southwest China and Northwest China were significantly worse than that of NCP.  
303 Generally, the poor predictive accuracy meant the higher RMSE and MAE when the absolute  
304 concentrations of  $\text{NO}_3^-$  for training samples were approximately equal. Moreover, most of the  
305 sampling sites in Southwest China were focused on Sichuan Basin, which often showed severe  $\text{NO}_3^-$   
306 pollution all the year round. Meanwhile, the annual mean  $\text{NO}_3^-$  concentrations in Yangling and  
307 Wuwei reached 4.1 and 4.5  $\mu\text{g}/\text{m}^3$ , respectively. The higher loadings of  $\text{NO}_3^-$  concentrations for



308 training samples led to the higher RMSE and MAE for Northwest China.

309 Although the cross-validation result suggested the new developed dataset achieved the better  
310 modelling accuracy, the cross-validation algorithm cannot test the transferability and agreement of  
311 this dataset in the past years. Hence, the unlearning data (annual mean  $\text{NO}_3^-$  concentration in 10  
312 cities) collected from previous references were employed to validate the transferability of this  
313 product. As shown in Fig. 4, we found that the  $R^2$  value of new-developed  $\text{NO}_3^-$  product and  
314 historical data reached 0.85 (Fig. 4), and the out-of-range  $R^2$  value was even slightly higher than the  
315 cross-validation  $R^2$  value. Moreover, the out-of-bag slope based on these unlearning data reached  
316 0.81, and equaled to the slope of cross-validation database. The result suggested the new-developed  
317 dataset showed excellent performance in the past decade.

318 Owing to the severe air pollution issue frequently observed in recent years, especially nitrogen-  
319 bearing haze events, many studies have tried to predict the  $\text{NO}_3^-$  concentrations in China. Most of  
320 these studies employed CTMs to simulate the ambient  $\text{NO}_3^-$  concentrations over China. Huang et al.  
321 (2015) employed WRF-CMAQ to estimate the inorganic nitrogen deposition over PRD, and  
322 confirmed that the R value only reached 0.54. Afterwards, Han et al. (2017) used RAMS-GMAQ to  
323 predict the dry deposition flux of reactive nitrogen, and significantly underestimated the  $\text{NO}_3^-$   
324 concentration in the atmosphere. Very recently, Geng et al. (2019) used CMAQ to estimate the  $\text{NO}_3^-$   
325 concentrations over East China, and the predictive performance ( $R = 0.53$ ) showed the similar result  
326 to Huang et al. (2015). Apart from these CTMs, the statistical models also has been applied to  
327 estimate the ambient  $\text{NO}_3^-$  concentration over China. Unfortunately, the predictive accuracy was not  
328 good based on traditional statistical models (e.g., linear regression) ( $R = 0.47$ ) (Jia et al., 2016). In  
329 terms of model performance, the developed  $\text{NO}_3^-$  product in our study was much better than those



330 developed by pioneering studies. Furthermore, this product showed many extra advantages than  
331 those obtained by CTMs especially for the hindcast of air pollutants. For instance, CTMs generally  
332 required continuous emission inventory data, which were often not available and showed high  
333 uncertainties. Moreover, CTMs generally needed substantial computing time and big-data input data  
334 to ensure the reliable predictive accuracy. Thus, the  $\text{NO}_3^-$  product retrieved by CTMs often lacks of  
335 long-term dataset (> 10 yr), and our study fills the gaps of previous studies.

#### 336 4.3 Spatial pattern of new-developed $\text{NO}_3^-$ dataset

337 The monthly  $\text{NO}_3^-$  concentration displayed the similar distribution characteristic with  $\text{PM}_{2.5}$  and  
338  $\text{PM}_{10}$  (Wei et al., 2019). Overall, the  $\text{NO}_3^-$  concentration in East China was much higher than that in  
339 West China. The higher  $\text{NO}_3^-$  concentration was concentrated on NCP ( $3.55 \pm 1.25 \mu\text{g}/\text{m}^3$ ), followed  
340 by Yangtze River Delta (YRD ( $2.56 \pm 1.12 \mu\text{g}/\text{m}^3$ )), Pearl River Delta (PRD ( $1.68 \pm 0.81 \mu\text{g}/\text{m}^3$ )),  
341 Sichuan Basin ( $1.53 \pm 0.63 \mu\text{g}/\text{m}^3$ ), and the lowest one observed in Tibetan Plateau ( $0.42 \pm 0.25$   
342  $\mu\text{g}/\text{m}^3$ ) (Fig. 5). Most provinces over NCP such as Beijing, Hebei, Henan, and Shandong suffered  
343 from severe  $\text{NO}_3^-$  pollution due to dense human activities and strong industry foundation (Li et al.,  
344 2017), which released a large amount of N-bearing gaseous pollutants to the atmosphere especially  
345 in winter. In BTH ( $2.97 \pm 1.97 \mu\text{g}/\text{m}^3$ ), Wang et al. (2016) verified that these fresh  $\text{NO}_x$  emitted from  
346 power plants or cement industries could be transformed into the nitrate in the particulate phase by  
347 the aid of low air temperature. In YRD and PRD, the combustion of fossil fuels and traffic emissions  
348 were considered to be the major source of  $\text{NO}_x$  emission, which favored to the formation of nitrate  
349 event through the gas-particle conversion processes (Fu et al., 2017; Kong et al., 2020; Ming et al.,  
350 2017). Apart from the contributions of smelting industries, the poor topographical or meteorological  
351 conditions were also responsible for the severe  $\text{NO}_3^-$  pollution in Sichuan Basin (Tian et al., 2017;





352 Wang et al., 2017). Tibetan Plateau generally showed the clean air quality due to the unique landform  
353 and scarce industrial activity (Yang et al., 2018). In addition, it was interesting to note that the Altai  
354 region and Taklimakan desert in Xinjiang autonomous region also showed some  $\text{NO}_3^-$  hotspots,  
355 though these regions were often believed to be the remote region. It was assumed that the many  
356 petrochemical industries (e.g., Karamai oil field) were located in the Altai region (Liu et al., 2018).  
357 Besides, Qi et al. (2018) verified that the resuspension of soil dust might trigger the accumulation  
358 of  $\text{NO}_3^-$  concentration in the aerosol.

#### 359 4.4 Long-term trend of ambient $\text{NO}_3^-$ across China

360 The temporal variation of  $\text{NO}_3^-$  levels from 2005 to 2015 over China has been clarified in Fig.  
361 6, Fig. 7 and Table S2. Overall, the ambient  $\text{NO}_3^-$  concentration in China showed the significant  
362 increasing trend of  $0.10 \mu\text{g}/\text{m}^3/\text{year}$  during 2005-2014, while it decreased sharply from 2014 to 2015  
363 by the speed of  $-0.40 \mu\text{g}/\text{m}^3/\text{year}$ . Overall, more than 90% areas of Mainland China showed  
364 consistent temporal variation with the gradual increase from 2005 to 2013, and then rapid decrease  
365 from 2013/2014 to 2015. However, the decreasing/increasing speed displayed significantly spatial  
366 difference in some major regions of China. For instance, the ambient  $\text{NO}_3^-$  level in BTH showed the  
367 remarkable increase during 2005-2014 by the speed of  $0.13 \mu\text{g}/\text{m}^3/\text{year}$ . Afterwards, the  $\text{NO}_3^-$  level  
368 decreased rapidly from 2014 to 2015 at a speed of  $-0.76 \mu\text{g}/\text{m}^3/\text{year}$ . The  $\text{NO}_3^-$  concentrations in  
369 YRD ( $0.08 \mu\text{g}/\text{m}^3/\text{year}$ ) and PRD ( $0.05 \mu\text{g}/\text{m}^3/\text{year}$ ) both showed the slight increases during 2005-  
370 2014, though the statistical test revealed the increases were significant ( $p < 0.05$ ). However, the  
371  $\text{NO}_3^-$  concentrations in YRD and PRD showed the dramatic decreases with  $-0.79$  and  $-0.59$   
372  $\mu\text{g}/\text{m}^3/\text{year}$ , respectively. As seen from 2005 to 2015, the  $\text{NO}_3^-$  concentration in BTH displayed the  
373 slight increase during this period. Nevertheless, the  $\text{NO}_3^-$  levels in YRD and PRD both displayed



374 the slow decreases by the speed of  $-0.01$  and  $-0.03 \mu\text{g}/\text{m}^3/\text{year}$ , respectively.

375 Furthermore, the different provinces displayed disparate temporal variations especially during  
376 11th five year plan (2005-2010). 31 provinces (municipalities/autonomous region) of China can be  
377 classified into three clusters based on the temporal trends of  $\text{NO}_3^-$  concentrations during 11th five  
378 year plan. The first cluster featured the gradual increase of  $\text{NO}_3^-$  concentration during this period,  
379 which consisted of three provinces in Northeast China (e.g., Heilongjiang) and central provinces in  
380 South China (e.g., Jiangxi, Anhui) (Table S2). The second cluster represented the provinces with the  
381 stable increases of  $\text{NO}_3^-$  during 2005-2007 and slight decreases during 2007-2010. Some provinces  
382 of NCP (e.g., Beijing, Hebei, Henan) and Northwest China (e.g., Gansu, Inner Mongolia, Ningxia)  
383 fell into the second cluster. The last cluster featured the opposite temporal trend to the second cluster  
384 during 2005-2010, which included many southern provinces such as Fujian, Guangdong, Zhejiang,  
385 and Guangxi. Although the central government proposed the emission reduction goal in 2006, the  
386 ambient  $\text{NO}_3^-$  concentrations in most provinces did not display pronounced decreases, which was  
387 totally different from the decrease of  $\text{PM}_{2.5}$  since 2007 (Xue et al., 2019). Especially in the provinces  
388 of Northeast China (e.g., Liaoning), the ambient  $\text{NO}_3^-$  concentrations in these provinces still showed  
389 the rapid increases after the proposal of emission control measures. It was assumed that these  
390 provinces generally possessed a large amount of energy-intensive industries and coal-fired power  
391 plants (Zhang et al., 2018). Moreover, the result might be associated with the fact that the emission  
392 reduction measures focused on the reduction of  $\text{SO}_2$  emission rather than  $\text{NO}_x$  emission (Kanada et  
393 al., 2013). Schreifels et al. (2012) revealed that major control measures during this period included  
394 shutting down inefficient industries, increasing the pollution levy for excessive  $\text{SO}_2$  emissions, and  
395 implementing energy conservation projects. Therefore, the total  $\text{SO}_2$  emission in 2010 decreased by



396 more than 14% compared with the emission in 1995 and the ambient SO<sub>2</sub> concentrations in many  
397 provinces since 2005 displayed significant decreases compared with those in 1990s (Li et al., 2020b;  
398 Lu et al., 2013; Zhou et al., 2015). Nonetheless, the NO<sub>x</sub> emission in China did not display  
399 significant decrease during this period (Duncan et al., 2016; Granier et al., 2017), and thus the  
400 ambient NO<sub>3</sub><sup>-</sup> in many provinces still kept the higher concentrations. It should be noted that the  
401 NO<sub>3</sub><sup>-</sup> concentrations in some provinces of NCP exactly exhibited the slow decreases after 2007. It  
402 was supposed that the energy structure adjustment and elimination of backward production capacity  
403 promoted the small decrease of NO<sub>3</sub><sup>-</sup> concentrations (Ma et al., 2019). Unfortunately, the slight  
404 decreases were quickly offset by the rapid increase of energy consumption. Zhang et al. (2018)  
405 demonstrated that the industry added values and private car number in BTH have been increasing  
406 by 189.4% and 279.6% during 2005-2010, respectively.

407 Since 2010, the central government began to implement severe limitations in PM<sub>2.5</sub>, NO<sub>x</sub>, and  
408 soot emissions, and thus the total NO<sub>x</sub> emission during 11th five year plan (2011-2015) showed  
409 slow decrease (10%) across China (Ma et al., 2019). However, the NO<sub>3</sub><sup>-</sup> concentrations across China  
410 did not show rapid response to the emission control measures. For instance, the NO<sub>3</sub><sup>-</sup> concentrations  
411 in most provinces of China still showed rapid increases during 2010-2013 (2014) (Fig. 7 and Fig.  
412 8). The result suggested that the control measures about the NO<sub>x</sub> emissions from vehicles and ships  
413 might be not very effective. Until 2013, the central government issued Action Plan for Air Pollution  
414 Prevention and Control (APPC-AP) in order to enhance the air pollution prevention measures (Li et  
415 al., 2017; Li et al., 2019). Many powerful economic and policy means including pricing (tax) policy  
416 and optimization of industrial layout caused the rapid decreases of NO<sub>3</sub><sup>-</sup> concentrations after 2013  
417 in many provinces (e.g., Beijing, Hebei, Zhejiang). Wang et al. (2019b) also verified that the NO<sub>3</sub><sup>-</sup>



418 level in  $PM_{2.5}$  over BTH has decreased by 20% during 2013-2015, which was in accordance with  
419 the finding of our study. In addition to the impact of emission reduction, the rapid decrease of  $NO_3^-$   
420 concentration over China after 2013 might be linked with the beneficial meteorological factors  
421 because Chen et al. (2019c) has demonstrated that favorable meteorological conditions led to about  
422 20 % of the  $PM_{2.5}$  decrease in BTH during 2014-2015. However, the decreasing trend of  $NO_3^-$   
423 concentration during 2014-2015 in PRD ( $-0.59 \mu\text{g}/\text{m}^3/\text{year}$ ) was significantly slower than that in  
424 BTH ( $-0.76 \mu\text{g}/\text{m}^3/\text{year}$ ) and YRD ( $-0.79 \mu\text{g}/\text{m}^3/\text{year}$ ) (Table 4). Wang et al. (2019b) found that the  
425 ambient  $NO_3^-$  concentration in a background site of PRD even showed an upward trend during 2014-  
426 2016. Thus, it was necessary to strengthen the control of nitrogen oxide emissions.

427 In general, the ambient  $NO_3^-$  concentration varied greatly at the seasonal scale (Fig. 9). China  
428 undergone the most serious  $NO_3^-$  pollution in winter ( $1.57 \pm 0.63 \mu\text{g}/\text{m}^3$ ), followed by autumn ( $1.09$   
429  $\pm 0.52 \mu\text{g}/\text{m}^3$ ), spring ( $0.78 \pm 0.50 \mu\text{g}/\text{m}^3$ ), and the lowest one in summer ( $0.63 \pm 0.40 \mu\text{g}/\text{m}^3$ ) (Table  
430 S3). The higher  $NO_3^-$  concentration observed in winter might be contributed by the dense coal  
431 combustion in North China and unfavorable meteorological conditions (Itahashi et al., 2017; Quan  
432 et al., 2014; Wang et al., 2019d). The lightest  $NO_3^-$  pollution in summer was attributable to the  
433 abundant precipitation, which promoted the diffusion and removal of pollutants and reduced  
434 ambient  $NO_3^-$  level (Hu et al., 2005). The ratio of  $NO_3^-$  concentration in winter ( $NO_{3^-}^{\text{winter}}$ ) and that  
435 in summer ( $NO_{3^-}^{\text{summer}}$ ) varied greatly at the spatial scale. The  $NO_{3^-}^{\text{winter}}/NO_{3^-}^{\text{summer}}$  in some  
436 provinces (municipalities) including Tianjin (2.11), Hebei (2.25), and Henan (2.84) displayed the  
437 higher values compared with other provinces. The higher  $NO_{3^-}^{\text{winter}}/NO_{3^-}^{\text{summer}}$  in NCP might be  
438 affected by the fossil fuel combustion for domestic heating, while some southern provinces did not  
439 need domestic heating in winter. In contrast, the ratio of  $NO_{3^-}^{\text{winter}}/NO_{3^-}^{\text{summer}}$  exhibited the lower



440 values in some western provinces such as Tibet and Qinghai. It might be probabaly associated with  
441 the less aerosol emission from anthropogenic source and the higher wind speed (Wei et al., 2019).

#### 442 4.5 Uncertainty analysis of $\text{NO}_3^-$ estimation

443 The ensemble model of three machine-learning algorithms captured the better accuracy in  
444 predicting the  $\text{NO}_3^-$  level from OMI data. Nonetheless, the ensemble model still showed some  
445 improvement space in terms of the  $R^2$  value. At first, meteorological data collected from reanalysis  
446 in ECMWF website generally showed high uncertainty, which inevitably increased the error of  $\text{NO}_3^-$   
447 estimation. In our study, we validated the gridded  $T_{2m}$  and  $T_p$  datasets against the groud-observed  
448 datasets and found that the  $R^2$  values of  $T_{2m}$  and  $T_p$  reached 0.98 and 0.83 (Table S4), respectively.  
449 The result suggested that  $T_{2m}$  showed the lower uncertainty, while  $T_p$  displayed relatively higher  
450 uncertainty. Except  $T_{2m}$  and  $T_p$ , the ground-level datasets for other meteorological factors were not  
451 open access, and thus we cannot assess their uncertainties. Thus, we only reviewed some references  
452 and evaluated their uncertainties. For instance, Guo et al. 2019 found that the reanalysis BLH data  
453 also exhibited large uncertainties because few sounding data were assimilated. These uncertainties  
454 derived from predictors could be passed to the ensemble model, and thus increased the uncertainties  
455 of ambient  $\text{NO}_3^-$  estimates.

456 The second reason was closely linked to the missing  $\text{NO}_2$  column amount across China. The  
457  $\text{NO}_2$  column amount retrieval showed many nonrandom biases especially for the arid or semi-arid  
458 area with high surface reflectance. The missing  $\text{NO}_2$  column amounts over China were not filled in  
459 our study due to the increased uncertainty of filling  $\text{NO}_2$  column. Moreover, it should be noted that  
460 the monthly  $\text{NO}_2$  column amounts were averaged based on the daily one, and the missing ratio of  
461 daily  $\text{NO}_2$  columns during 2005-2015 reached 57.64%, the higher missing ratio might increase the



462 uncertainty of  $\text{NO}_3^-$  simulation.

463 Lastly, the developed ensemble model did not integrate the direct spatiotemporal weight  
464 indicators (e.g., the distance of observed sites and contiguous grids) though many predictors (e.g.,  
465 month of year) reflecting spatiotemporal autocorrelation were input into the original model as the  
466 key predictors. Furthermore, the developed model was the ensemble one of three original models,  
467 which ignored the spatiotemporal autocorrelation of estimation residues from first-stage model. In  
468 the future work, the ensemble model could be combined with a space-time model to further enhance  
469 the modelling performance.

#### 470 **5. Data availability**

471 The monthly  $\text{NO}_3^-$  datasets at  $0.25^\circ$  resolution across China during 2005-2015 are available at  
472 <https://doi.org/10.5281/zenodo.3988307> (Li et al., 2020), which can be downloaded in xlsx format.  
473 The missing values are shown in NaN.

#### 474 **6. Conclusions and implications**

475 In this study, RF, GBDT, and XGBoost algorithms were combined to establish a high-resolution  
476 ( $0.25^\circ$ )  $\text{NO}_3^-$  dataset over China during 2005-2015 on the basis of multi-source predictors. The  $\text{NO}_3^-$   
477 product showed high cross-validation  $R^2$  value (0.78), but low RMSE ( $1.19 \mu\text{g}/\text{m}^3$ ) and MAE ( $0.81$   
478  $\mu\text{g}/\text{m}^3$ ). The  $\text{NO}_3^-$  dataset showed the markedly spatiotemporal discrepancy. The  $R^2$  value was in the  
479 order of summer (0.85) > spring (0.80) = autumn (0.80) > winter (0.75) across China, and the  $R^2$   
480 showed the highest value in NCP. In addition, the dataset exhibited excellent transferability ( $R^2 =$   
481  $0.85$ , RMSE =  $0.74 \mu\text{g}/\text{m}^3$ , and MAE =  $0.55 \mu\text{g}/\text{m}^3$ ) on the basis of the unlearning observed data in  
482 ten sites.

483 The new-developed  $\text{NO}_3^-$  dataset showed remarkably predictive accuracy compared with



484 previous products developed by CTMs and linear regression model. The result might be linked to  
485 two key reasons. First of all, the new product assimilated high-resolution NO<sub>2</sub> column amount  
486 instead of the NO<sub>x</sub> emission inventory used by CTMs. The imperfect knowledge about the chemical  
487 modules with regard of the NO<sub>3</sub><sup>-</sup> formation and the inaccurate emission inventory decreased the  
488 predictive performance of CTMs. In contrast, the new product was obtained using ensemble  
489 machine-learning model, which did not need to consider the photochemical or aqueous process from  
490 gaseous NO<sub>2</sub> to particulate NO<sub>3</sub><sup>-</sup>. Compared with the NO<sub>3</sub><sup>-</sup> product estimated by linear regression  
491 model ( $R^2 = 0.21$ ), the new product significantly elevated the modelling performance of NO<sub>3</sub><sup>-</sup>  
492 concentration. It was supposed that the ensemble model for the development of the new NO<sub>3</sub><sup>-</sup> dataset  
493 did not predefine the potential relationships between explanatory variables and NO<sub>3</sub><sup>-</sup> level as the  
494 multiple regression model, which must assume the linear linkage between dependent variable and  
495 predictors before model establishment.

496 On the basis of the such dataset, the spatiotemporal variation of NO<sub>3</sub><sup>-</sup> concentration over China  
497 during 2005-2015 were clarified. The annual mean NO<sub>3</sub><sup>-</sup> concentration followed the order of NCP  
498 ( $3.55 \pm 1.25 \mu\text{g}/\text{m}^3$ ) > YRD ( $2.56 \pm 1.12 \mu\text{g}/\text{m}^3$ ) > PRD ( $1.68 \pm 0.81 \mu\text{g}/\text{m}^3$ ) > Sichuan Basin ( $1.53$   
499  $\pm 0.63 \mu\text{g}/\text{m}^3$ ) > Tibetan Plateau ( $0.42 \pm 0.25 \mu\text{g}/\text{m}^3$ ). The higher NO<sub>3</sub><sup>-</sup> concentrations in NCP, YRD,  
500 and PRD were mainly contributed by the intensive industrial and traffic emissions. Sichuan Basin  
501 suffered serious NO<sub>3</sub><sup>-</sup> pollution due to the high loadings of aerosols and unfavorable terrain  
502 condition. Tibetan Plateau shared with the lightest NO<sub>3</sub><sup>-</sup> pollution because of the scarce  
503 anthropogenic emissions and favorable meteorological factors. Additionally, we also found that the  
504 ambient NO<sub>3</sub><sup>-</sup> concentration showed significant increasing trend of  $0.10 \mu\text{g}/\text{m}^3/\text{year}$  during 2005-  
505 2014, while it decreased sharply from 2014 to 2015 at a speed of  $-0.40 \mu\text{g}/\text{m}^3/\text{year}$ . The ambient



506  $\text{NO}_3^-$  levels in BTH, YRD, and PRD displayed slight increases at the speed of 0.13, 0.08, and 0.03  
507  $\mu\text{g}/\text{m}^3/\text{year}$ , respectively. Afterwards, the  $\text{NO}_3^-$  concentrations decreased sharply at the speed of -  
508 0.76, -0.79, and -0.59  $\mu\text{g}/\text{m}^3/\text{year}$ . Although National Economic and Social Development of China  
509 has issued the emission reduction goal in 2006, the  $\text{NO}_3^-$  concentrations in most provinces did not  
510 show the significant decreases during 2005-2010. It might be contributed by the increase of energy  
511 consumption and non-targeted emission control measures. Since 2010, the government began to  
512 decrease the  $\text{NO}_x$  emission over China, whereas the  $\text{NO}_3^-$  concentrations in many provinces still  
513 showed slight increases during 2010-2014 because the benefits of control measures for  $\text{NO}_x$   
514 emission could be neutralized by elevated energy consumption along with the rapid economic  
515 development. After 2014, Chinese government issued APPC-AP and further enhanced the emission  
516 control measures, and triggered the dramatic decrease of  $\text{NO}_3^-$  concentration over China. Apart from  
517 the effect of emission reduction, the favorable meteorological conditions might lead to the rapid  
518 decrease of  $\text{NO}_3^-$  level over China during 2014-2015. Compared with the powerful emission control  
519 measures, meteorological factors only contributed a small portion of  $\text{NO}_3^-$  reduction in China.  
520 Besides, the decrease speed of  $\text{NO}_3^-$  level in China also displayed pronounced spatial heterogeneity  
521 and some background region even featured the upward of air pollutant in recent years. Therefore, it  
522 is still imperative to strengthen the emission reduction measures.

523 It must be acknowledged that our study still suffers from some limitations. First of all, the  $\text{NO}_3^-$   
524 dataset was developed by machine-learning models, which lacked of the chemical module  
525 concerning about the transformation pathway from  $\text{NO}_2$  to  $\text{NO}_3^-$ , and might underestimate the  
526 ambient  $\text{NO}_3^-$  concentration across China. In the future work, the output results of CTMs including  
527 conversion ratio from  $\text{NO}_2$  to  $\text{NO}_3^-$ , dry/wet deposition flux of  $\text{NO}_2$  and  $\text{NO}_3^-$  in the atmosphere





528 should be incorporated into the machine-learning model to develop next-generation  $\text{NO}_3^-$  product.  
529 Second, the low time-resolution (monthly) observation data hindered the daily estimation of  $\text{NO}_3^-$   
530 concentration. The daily  $\text{NO}_3^-$  datasets are warranted in the future because it could be used to assess  
531 the potential impact on human health. Besides, the ultrahigh-resolution satellite (TROPOMI) can  
532 allow continuation and enhancement of the spatiotemporal  $\text{NO}_3^-$  estimation though the OMI product  
533 could capture enough spatial variations across China.

#### 534 **Acknowledgements**

535 This work was funded by Chinese Postdoctoral Science Foundation (2020M680589) and National  
536 Natural Science Foundation of China (Nos. 21777025).

#### 537 **Author contributions**

538 Rui Li, Lulu Cui, and Hongbo Fu conceived and designed the study. Rui Li, Lulu Cui, Yilong Zhao,  
539 Wenhui Zhou collected and processed the data. Rui Li wrote this paper with contributions from all  
540 of the coauthors.



541 **References**

- 542 Breiman, L.: Random forests. *Machine learning* 45, 5-32, 2001.
- 543 Chen, H., Li, D., Gurmesa, G.A., Yu, G., Li, L., Zhang, W., Fang, H., Mo, J.: Effects of nitrogen  
544 deposition on carbon cycle in terrestrial ecosystems of China: A meta-analysis. *Environ. Pollut.* 206,  
545 352-360, <https://doi.org/10.1016/j.envpol.2015.07.033>, 2015.
- 546 Chen, J., Yin, J., Zang, L., Zhang, T., Zhao, M.: Stacking machine learning model for estimating hourly  
547 PM<sub>2.5</sub> in China based on Himawari-8 aerosol optical depth data. *Sci. Total Environ.* 697, 134021,  
548 <https://doi.org/10.1016/j.scitotenv.2019.134021>, 2019a.
- 549 Chen, Z.Y., Zhang, R., Zhang, T.H., Ou, C.Q., Guo, Y.: A kriging-calibrated machine learning method  
550 for estimating daily ground-level NO<sub>2</sub> in mainland China. *Sci. Total Environ.* 690, 556-564,  
551 <https://doi.org/10.1016/j.scitotenv.2019.06.349>, 2019b.
- 552 Chen, Z., Chen, D., Kwan, M., Chen, B., Cheng, N., Gao, B., Zhuang, Y., Li, R., and Xu, B.: The control  
553 of anthropogenic emissions contributed to 80 % of the decrease in PM<sub>2.5</sub> concentrations in Beijing  
554 from 2013 to 2017, *Atmos. Chem. Phys. Discuss.*, <https://doi.org/10.5194/acp-2018-1112>, 2019c.
- 555 Compton, J.E., Harrison, J.A., Dennis, R.L., Greaver, T.L., Hill, B.H., Jordan, S.J., Walker, H., Campbell,  
556 H.V.: Ecosystem services altered by human changes in the nitrogen cycle: a new perspective for US  
557 decision making. *Ecology letters* 14, 804-815, <https://doi.org/10.1111/j.1461-0248.2011.01631.x>,  
558 2011.
- 559 Cui, S., Shi, Y., Malik, A., Lenzen, M., Gao, B., Huang, W.: A hybrid method for quantifying China's  
560 nitrogen footprint during urbanisation from 1990 to 2009. *Environ. Interna.* 97, 137-145,  
561 <https://doi.org/10.1016/j.envint.2016.08.012>, 2016.
- 562 Du, E., de Vries, W., Galloway, J.N., Hu, X., Fang, J.: Changes in wet nitrogen deposition in the United



- 563 States between 1985 and 2012. *Environ. Res. Lett.* 9, 095004, 2014.
- 564 Duncan, B.N., Lamsal, L.N., Thompson, A.M., Yoshida, Y., Lu, Z., Streets, D.G., Hurwitz, M.M.,  
565 Pickering, K.E.: A space-based, high-resolution view of notable changes in urban NO<sub>x</sub> pollution  
566 around the world (2005–2014). *J. Geophys. Res.* 121, 976–996, <https://doi.org/10.1002/2015JD024121>,  
567 2016.
- 568 Erisman, J.W., Galloway, J.N., Seitzinger, S., Bleeker, A., Dise, N.B., Petrescu, A.R., Leach, A.M., de  
569 Vries, W.: Consequences of human modification of the global nitrogen cycle. *Philosophical  
570 Transactions of the Royal Society B: Biological Sciences* 368, 20130116,  
571 <https://doi.org/10.1098/rstb.2013.0116>, 2013.
- 572 Fu, H., Chen, J.: Formation, features and controlling strategies of severe haze-fog pollutions in China.  
573 *Sci. Total Environ.* 578, 121–138, <https://doi.org/10.1016/j.scitotenv.2016.10.201>, 2017.
- 574 Fu, X., Wang, S., Xing, J., Zhang, X., Wang, T., Hao, J.: Increasing ammonia concentrations reduce the  
575 effectiveness of particle pollution control achieved via SO<sub>2</sub> and NO<sub>x</sub> emissions reduction in east China.  
576 *Environ. Sci. Tech. Lett.* 4, 221–227, <https://doi.org/10.1021/acs.estlett.7b00143>, 2017.
- 577 Georgoulias, A. K., van der A, R. J., Stammes, P., Boersma, K. F., and Eskes, H. J.: Trends and trend  
578 reversal detection in 2 decades of tropospheric NO<sub>2</sub> satellite observations, *Atmos. Chem. Phys.*, 6269–  
579 6294, <https://doi.org/10.5194/acp-19-6269-2019>, 2019.
- 580 Granier, C., Granier, L., Sindelarova, K., Lioussé, C., Darras, S., Bouarar, I., van der Gon, H.D., Frost,  
581 G.J., Janssens-Maenhout, G., Crippa, M.: Trends in anthropogenic emissions from 1960 to 2015. *Hal.  
582 Archives*, 2017.
- 583 Guo, J., Su, T., Chen, D., Wang, J., Li, Z., Lv, Y., Guo, X., Liu, H., Cribb, M., Zhai, P.: Declining  
584 Summertime Local-Scale Precipitation Frequency Over China and the United States, 1981–2012. *The*



585 Disparate Roles of Aerosols. *Geophys. Res. Lett.* 46, 13281-13289,  
586 <https://doi.org/10.1029/2019GL085442>, 2019.

587 Han, X., Zhang, M., Skorokhod, A., Kou, X.: Modeling dry deposition of reactive nitrogen in China with  
588 RAMS-CMAQ. *Atmos. Environ.* 166, 47-61, <https://doi.org/10.1016/j.atmosenv.2017.07.015>, 2017.

589 Hu, M., Zhang, J., Wu, Z.: Chemical compositions of precipitation and scavenging of particles in Beijing.  
590 *Sci. China B* 48, 265-272, *Science in China Series B: Chemistry*, 2005.

591 Huang, Z., Wang, S., Zheng, J., Yuan, Z., Ye, S., Kang, D.: Modeling inorganic nitrogen deposition in  
592 Guangdong province, China. *Atmos. Environ.* 109, 147-160,  
593 <https://doi.org/10.1016/j.atmosenv.2015.03.014>, 2015.

594 Itahashi, S., Uno, I., Osada, K., Kamiguchi, Y., Yamamoto, S., Tamura, K., Wang, Z., Kurosaki, Y.,  
595 Kanaya, Y.: Nitrate transboundary heavy pollution over East Asia in winter. *Atmos. Chem. Phys.* 17,  
596 3823-3843, 2017.

597 Jia, Y., Yu, G., Gao, Y., He, N., Wang, Q., Jiao, C., Zuo, Y.: Global inorganic nitrogen dry deposition  
598 inferred from ground-and space-based measurements. *Sci. Rep.* 6, 19810, [10.1038/srep19810](https://doi.org/10.1038/srep19810), 2016.

599 Kanada, M., Dong, L., Fujita, T., Fujii, M., Inoue, T., Hirano, Y., Togawa, T., Geng, Y.: Regional disparity  
600 and cost-effective SO<sub>2</sub> pollution control in China: A case study in 5 mega-cities. *Energ. Policy* 61,  
601 1322-1331, <https://doi.org/10.1016/j.enpol.2013.05.105>, 2013.

602 Kong, L., Hu, M., Tan, Q., Feng, M., Qu, Y., An, J., Zhang, Y., Liu, X., Cheng, N.: Aerosol optical  
603 properties under different pollution levels in the Pearl River Delta (PRD) region of China. *J. Environ.*  
604 *Sci.* 87, 49-59, <https://doi.org/10.1016/j.jes.2019.02.019>, 2020.

605 Kong, L., Tang, X., Zhu, J., Wang, Z.F., Li, J.J., Wu, H.J., Carmichael, G.R.: A Six-year long (2013–  
606 2018) High-resolution Air Quality Reanalysis Dataset over China based on the assimilation of surface



- 607 observations from CNEMC. Earth Sys. Sci. Data, <https://doi.org/10.5194/essd-2020-100>, 2019.
- 608 Li, R., Cui, L., Hongbo, F., Li, J., Zhao, Y., Chen, J.: Satellite-based estimation of full-coverage ozone  
609 (O<sub>3</sub>) concentration and health effect assessment across Hainan Island. J. Cleaner Prod. 244, 118773,  
610 <https://doi.org/10.1016/j.jclepro.2019.118773>, 2020a.
- 611 Li, R., Cui, L., Li, J., Zhao, A., Fu, H., Wu, Y., Zhang, L., Kong, L., Chen, J.: Spatial and temporal  
612 variation of particulate matter and gaseous pollutants in China during 2014-2016. Atmos. Environ.  
613 161, 235-246, <https://doi.org/10.1016/j.atmosenv.2017.05.008>, 2017.
- 614 Li, R., Cui, L., Liang, J., Zhao, Y., Zhang, Z., Fu, H.: Estimating historical SO<sub>2</sub> level across the whole  
615 China during 1973–2014 using random forest model. Chemosphere, 125839,  
616 <https://doi.org/10.1016/j.chemosphere.2020.125839>, 2020b.
- 617 Li, R., Wang, Z., Cui, L., Fu, H., Zhang, L., Kong, L., Chen, W., Chen, J.: Air pollution characteristics  
618 in China during 2015–2016: Spatiotemporal variations and key meteorological factors. Sci. Total  
619 Environ. 648, 902-915, <https://doi.org/10.1016/j.scitotenv.2018.08.181>, 2019.
- 620 Li, R., Cui, L.L., Zhao, Y.L., Zhou, W.H., Fu, H.B.: Long-term trends of ambient nitrate (NO<sub>3</sub>-)  
621 concentrations across China based on ensemble machine-learning models,  
622 <https://doi.org/10.5281/zenodo.3988307>, 2020c.
- 623 Liu, L., Zhang, X., Xu, W., Liu, X., Li, Y., Lu, X., Zhang, Y., Zhang, W.: Temporal characteristics of  
624 atmospheric ammonia and nitrogen dioxide over China based on emission data, satellite observations  
625 and atmospheric transport modeling since 1980. Atmos. Chem. Phys. 17, 9365-9378, 2017a.
- 626 Liu, X., Duan, L., Mo, J., Du, E., Shen, J., Lu, X., Zhang, Y., Zhou, X., He, C., Zhang, F.: Nitrogen  
627 deposition and its ecological impact in China: an overview. Environ. Pollut. 159, 2251-2264,  
628 <https://doi.org/10.1016/j.envpol.2010.08.002>, 2011.



- 629 Liu, X., Xu, W., Duan, L., Du, E., Pan, Y., Lu, X., Zhang, L., Wu, Z., Wang, X., Zhang, Y.: Atmospheric  
630 nitrogen emission, deposition, and air quality impacts in China: An overview. *Curr. Pollut. Rep.* 3, 65-  
631 77, 2017b.
- 632 Liu, Z., Gao, W., Yu, Y., Hu, B., Xin, J., Sun, Y., Wang, L., Wang, G., Bi, X., Zhang, G.: Characteristics  
633 of PM<sub>2.5</sub> mass concentrations and chemical species in urban and background areas of China: emerging  
634 results from the CARE-China network. *Atmos. Chem. Phys.* 18, 1-34, [https://www.atmos-chem-](https://www.atmos-chem-phys.net/18/8849/2018/acp-18-8849-2018-discussion.html)  
635 [phys.net/18/8849/2018/acp-18-8849-2018-discussion.html](https://www.atmos-chem-phys.net/18/8849/2018/acp-18-8849-2018-discussion.html), 2018.
- 636 Lu, Z., Streets, D.G., de Foy, B., Krotkov, N.A.: Ozone Monitoring Instrument observations of  
637 interannual increases in SO<sub>2</sub> emissions from Indian coal-fired power plants during 2005-2012. *Environ.*  
638 *Sci. Tech.* 47, 13993-14000, <https://doi.org/10.1021/es4039648>, 2013.
- 639 Ma, Z., Liu, R., Liu, Y., Bi, J.: Effects of air pollution control policies on PM<sub>2.5</sub> pollution improvement  
640 in China from 2005 to 2017: a satellite-based perspective. *Atmos. Chem. Phys.* 19, 6861-6877,  
641 <https://doi.org/10.5194/acp-19-6861-2019>, 2019.
- 642 Ming, L., Jin, L., Li, J., Fu, P., Yang, W., Liu, D., Zhang, G., Wang, Z., Li, X.: PM<sub>2.5</sub> in the Yangtze River  
643 Delta, China: Chemical compositions, seasonal variations, and regional pollution events. *Environ.*  
644 *Pollut.* 223, 200-212, <https://doi.org/10.1016/j.envpol.2017.01.013>, 2017.
- 645 Qi, J., Liu, X., Yao, X., Zhang, R., Chen, X., Lin, X., Gao, H., Liu, R.: The concentration, source and  
646 deposition flux of ammonium and nitrate in atmospheric particles during dust events at a coastal site  
647 in northern China. *Atmos. Chem. Phys.* 18, 571, <https://doi.org/10.5194/acp-18-571-2018>, 2018.
- 648 Qiao, X., Xiao, W., Jaffe, D., Kota, S.H., Ying, Q., Tang, Y.: Atmospheric wet deposition of sulfur and  
649 nitrogen in Jiuzhaigou national nature reserve, Sichuan province, China. *Sci. Total Environ.* 511, 28-  
650 36, <https://doi.org/10.1016/j.scitotenv.2014.12.028>, 2015.



- 651 Qin, K., Zou, J., Guo, J., Lu, M., Bilal, M., Zhang, K., Ma, F., Zhang, Y.: Estimating PM<sub>1</sub> concentrations  
652 from MODIS over Yangtze River Delta of China during 2014-2017. *Atmos. Environ.* 195, 149-158,  
653 <https://doi.org/10.1016/j.atmosenv.2018.09.054>, 2018.
- 654 Quan, J., Tie, X., Zhang, Q., Liu, Q., Li, X., Gao, Y., Zhao, D.: Characteristics of heavy aerosol pollution  
655 during the 2012-2013 winter in Beijing, China. *Atmos. Environ.* 88, 83-89,  
656 <https://doi.org/10.1016/j.atmosenv.2014.01.058>, 2014.
- 657 Schreifels, J.J., Fu, Y., Wilson, E.J.: Sulfur dioxide control in China: policy evolution during the 10th and  
658 11th Five-year Plans and lessons for the future. *Energ. Policy* 48, 779-789,  
659 <https://doi.org/10.1016/j.enpol.2012.06.015>, 2012.
- 660 Shen, J., Li, Y., Liu, X., Luo, X., Tang, H., Zhang, Y., Wu, J.: Atmospheric dry and wet nitrogen  
661 deposition on three contrasting land use types of an agricultural catchment in subtropical central China.  
662 *Atmos. Environ.* 67, 415-424, <https://doi.org/10.1016/j.atmosenv.2012.10.068>, 2013.
- 663 Shen, J., Tang, A., Liu, X., Fangmeier, A., Goulding, K., Zhang, F.: High concentrations and dry  
664 deposition of reactive nitrogen species at two sites in the North China Plain. *Environ. Pollut.* 157,  
665 3106-3113, <https://doi.org/10.1016/j.envpol.2009.05.016>, 2009.
- 666 Singh, S., Sharma, A., Kumar, B., Kulshrestha, U.: Wet deposition fluxes of atmospheric inorganic  
667 reactive nitrogen at an urban and rural site in the Indo-Gangetic Plain. *Atmos. Pollut. Res.* 8, 669-677,  
668 <https://doi.org/10.1016/j.apr.2016.12.021>, 2017.
- 669 Tang, X.L., Fan, S.H., Du, M.Y., Zhang, W.J., Gao, S.C., Liu, S.B., Chen, G., Yu, Z., Yang, W.N.: Spatial  
670 and temporal patterns of global soil heterotrophic respiration in terrestrial ecosystems. *Earth Syst. Sci.*  
671 *Data* 12, 1037-1051, 2020.
- 672 Tian, M., Wang, H., Chen, Y., Zhang, L., Shi, G., Liu, Y., Yu, J., Zhai, C., Wang, J., Yang, F.: Highly time-



- 673 resolved characterization of water-soluble inorganic ions in PM<sub>2.5</sub> in a humid and acidic mega city in  
674 Sichuan Basin, China. *Sci. Total Environ.* 580, 224-234,  
675 <https://doi.org/10.1016/j.scitotenv.2016.12.048>, 2017.
- 676 Vrekoussis, M., Richter, A., Hilboll, A., Burrows, J., Gerasopoulos, E., Lelieveld, J., Barrie, L., Zerefos,  
677 C., Mihalopoulos, N.: Economic crisis detected from space: Air quality observations over  
678 Athens/Greece. *Geophys. Res. Lett.* 40, 458-463, <https://doi.org/10.1002/grl.50118>, 2013.
- 679 Wang, H., Shi, G., Tian, M., Zhang, L., Chen, Y., Yang, F., Cao, X.: Aerosol optical properties and  
680 chemical composition apportionment in Sichuan Basin, China. *Sci. Total Environ.* 577, 245-257,  
681 <https://doi.org/10.1016/j.scitotenv.2016.10.173>, 2017.
- 682 Wang, Q., Zhuang, G., Huang, K., Liu, T., Lin, Y., Deng, C., Fu, Q., Fu, J.S., Chen, J., Zhang, W.:  
683 Evolution of particulate sulfate and nitrate along the Asian dust pathway: Secondary transformation  
684 and primary pollutants via long-range transport. *Atmos. Res.* 169, 86-95,  
685 <https://doi.org/10.1016/j.atmosres.2015.09.013>, 2016.
- 686 Wang, W., Xu, W., Wen, Z., Wang, D., Wang, S., Zhang, Z., Zhao, Y., Liu, X.: Characteristics of  
687 Atmospheric Reactive Nitrogen Deposition in Nyingchi City. *Sci. Rep.* 9, 1-11,  
688 <https://xs.scihub.ltd/https://doi.org/10.1038/s41598-019-39855-2>, 2019a.
- 689 Wang, Y., Li, W., Gao, W., Liu, Z., Tian, S., Shen, R., Ji, D., Wang, S., Wang, L., Tang, G.: Trends in  
690 particulate matter and its chemical compositions in China from 2013–2017. *Sci. China Earth Sci.* 62,  
691 1857-1871, <https://xs.scihub.ltd/https://doi.org/10.1007/s11430-018-9373-1>, 2019b.
- 692 Wang, Y., Li, W., Gao, W., Liu, Z., Tian, S., Shen, R., Ji, D., Wang, S., Wang, L., Tang, G.: Trends in  
693 particulate matter and its chemical compositions in China from 2013–2017. *Sci. China Earth Sci.*, 1-  
694 15, <https://xs.scihub.ltd/https://doi.org/10.1007/s11430-018-9373-1>, 2019c.





- 695 Wang, Y.L., Song, W., Yang, W., Sun, X.C., Tong, Y.D., Wang, X.M., Liu, C.Q., Bai, Z.P., Liu, X.Y.  
696 Influences of atmospheric pollution on the contributions of major oxidation pathways to PM<sub>2.5</sub> nitrate  
697 formation in Beijing. *J. Geophys. Res.* 124, 4174-4185, <https://doi.org/10.1029/2019JD030284>, 2019d.
- 698 Wei, J., Huang, W., Li, Z., Xue, W., Peng, Y., Sun, L., Cribb, M.: Estimating 1-km-resolution PM<sub>2.5</sub>  
699 concentrations across China using the space-time random forest approach. *Remote Sens. Environ.* 231,  
700 111221, <https://doi.org/10.1016/j.rse.2019.111221>, 2019.
- 701 Wolpert, D.H.: Stacked generalization. *Neural networks* 5, 241-259, <https://doi.org/10.1016/S0893->  
702 [6080\(05\)80023-1](https://doi.org/10.1016/S0893-6080(05)80023-1), 1992.
- 703 Xu, W., Liu, L., Cheng, M., Zhao, Y., Zhang, L., Pan, Y., Zhang, X., Gu, B., Li, Y., Zhang, X.: Spatial-  
704 temporal patterns of inorganic nitrogen air concentrations and deposition in eastern China. *Atmos.*  
705 *Chem. Phys.* 18, 10931-10954, <https://doi.org/10.5194/acp-18-10931-2018>, 2018a.
- 706 Xu, W., Zhao, Y., Liu, X., Dore, A.J., Zhang, L., Liu, L., Cheng, M.: Atmospheric nitrogen deposition in  
707 the Yangtze River basin: Spatial pattern and source attribution. *Environ. Pollut.* 232, 546-555,  
708 <https://doi.org/10.1016/j.envpol.2017.09.086>, 2018b.
- 709 Xue, T., Zheng, Y.X., Tong, D., Zheng, B., Li, X., Zhu, T., Zhang, Q.: Spatiotemporal continuous  
710 estimates of PM<sub>2.5</sub> concentrations in China, 2000–2016: A machine learning method with inputs from  
711 satellites, chemical transport model, and ground observations. *Environ. Internat.* 123, 345-357,  
712 <https://doi.org/10.1016/j.envint.2018.11.075>, 2019.
- 713 Yang, J., Kang, S., Ji, Z.: Sensitivity analysis of chemical mechanisms in the WRF-chem model in  
714 reconstructing aerosol concentrations and optical properties in the Tibetan plateau. *Aerosol Air Qual.*  
715 *Res.* 18, 505-521, doi: 10.4209/aaqr.2017.05.0156, 2018.
- 716 Zang, L., Mao, F., Guo, J., Wang, W., Pan, Z., Shen, H., Zhu, B., Wang, Z.: Estimation of spatiotemporal



- 717 PM<sub>1.0</sub> distributions in China by combining PM<sub>2.5</sub> observations with satellite aerosol optical depth. *Sci.*  
718 *Total Environ.* 658, 1256-1264, <https://doi.org/10.1016/j.scitotenv.2018.12.297>, 2019.
- 719 Zhai, B.X., Chen, J.G.: Development of a stacked ensemble model for forecasting and analyzing daily  
720 average PM<sub>2.5</sub> concentrations in Beijing, China. *Sci. Total Environ.* 635, 644-658,  
721 <https://doi.org/10.1016/j.scitotenv.2018.04.040>, 2018.
- 722 Zhan, Y., Luo, Y., Deng, X., Chen, H., Grieneisen, M.L., Shen, X., Zhu, L., Zhang, M.: Spatiotemporal  
723 prediction of continuous daily PM<sub>2.5</sub> concentrations across China using a spatially explicit machine  
724 learning algorithm. *Atmos. Environ.* 155, 129-139, <https://doi.org/10.1016/j.atmosenv.2017.02.023>,  
725 2017.
- 726 Zhan, Y., Luo, Y., Deng, X., Grieneisen, M.L., Zhang, M., Di, B.: Spatiotemporal prediction of daily  
727 ambient ozone levels across China using random forest for human exposure assessment. *Environ.*  
728 *Pollut.* 233, 464-473, <https://doi.org/10.1016/j.envpol.2017.10.029>, 2018a.
- 729 Zhan, Y., Luo, Y., Deng, X., Zhang, K., Zhang, M., Grieneisen, M.L., Di, B.: Satellite-Based estimates  
730 of daily NO<sub>2</sub> exposure in China using hybrid random forest and spatiotemporal Kriging model.  
731 *Environ. Sci. Tech.* 52, 4180-4189, <https://doi.org/10.1021/acs.est.7b05669>, 2018b.
- 732 Zhao, Y., Zhang, L., Chen, Y., Liu, X., Xu, W., Pan, Y., Duan, L.: Atmospheric nitrogen deposition to  
733 China: A model analysis on nitrogen budget and critical load exceedance. *Atmos. Environ.* 153, 32-40,  
734 <https://doi.org/10.1016/j.atmosenv.2017.01.018>, 2017.
- 735 Zhang, X.Y., Zhang, W.T., Lu, X.H., Liu, X.J., Chen, D.M., Liu, L., Huang, X.J.: Long-term trends in  
736 NO<sub>2</sub> columns related to economic developments and air quality policies from 1997 to 2016 in China.  
737 *Sci. Total Environ.* 639, 146-155, <https://doi.org/10.1016/j.scitotenv.2018.04.435>, 2018.
- 738 Zhou, K., Yang, S., Shen, C., Ding, S., Sun, C.: Energy conservation and emission reduction of China's

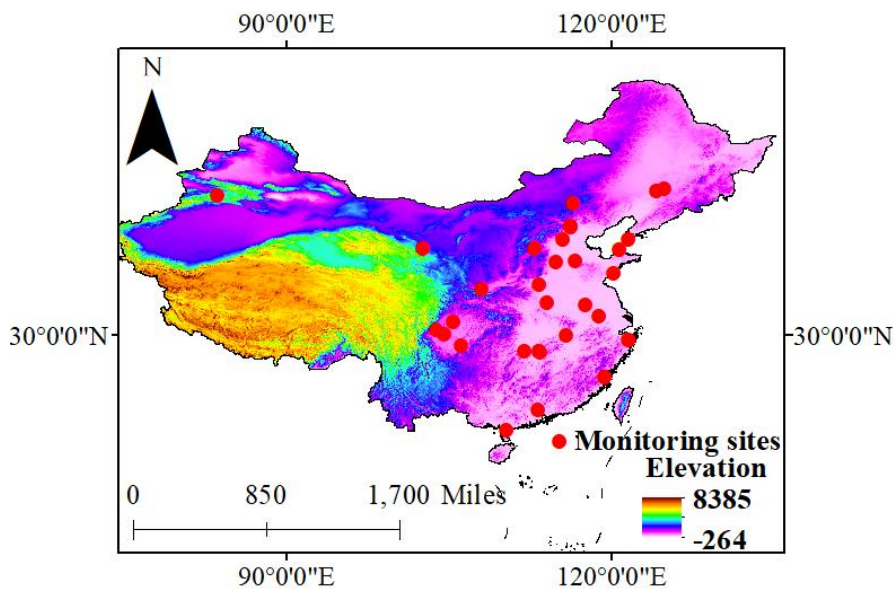


739 electric power industry. Renewable and Sustainable Energy Reviews 45, 10-19,

740 <https://doi.org/10.1016/j.rser.2015.01.056>, 2015.

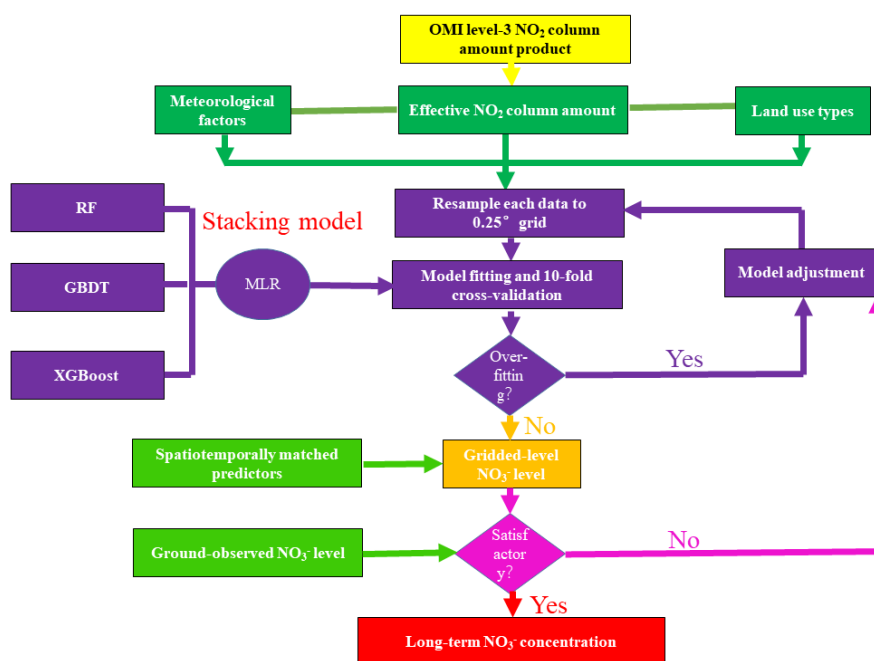


741 **Fig. 1** Spatial distributions of ground-level  $\text{NO}_3^-$  monitoring sites used for model establishment. Red  
742 circles represent the ground-level sites during 2010-2015. The colormap denotes the elevation  
743 distribution across China.





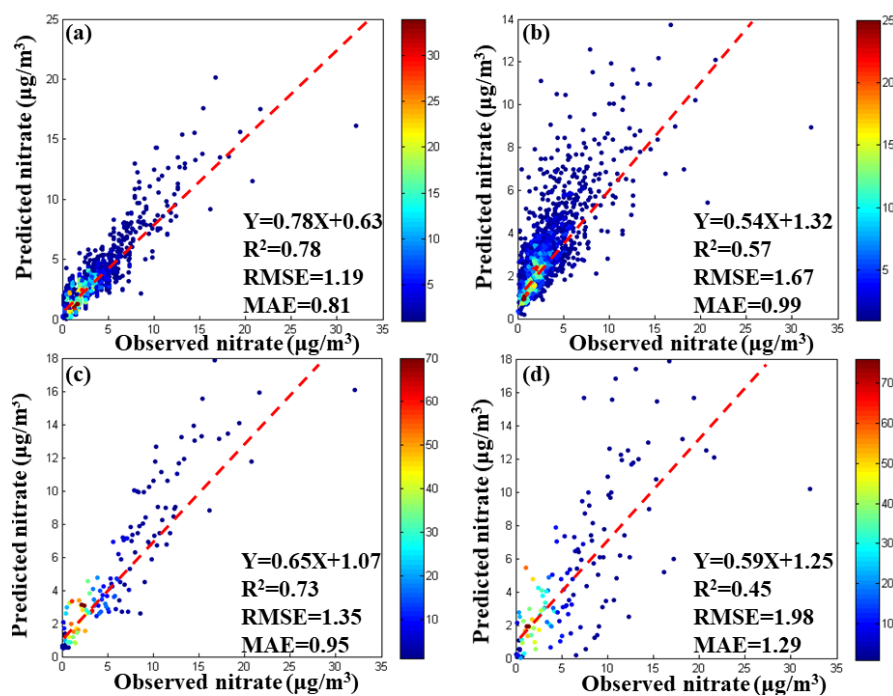
745 **Fig. 2** The workflow of the ensemble model development for ambient  $\text{NO}_3^-$  estimates.



746



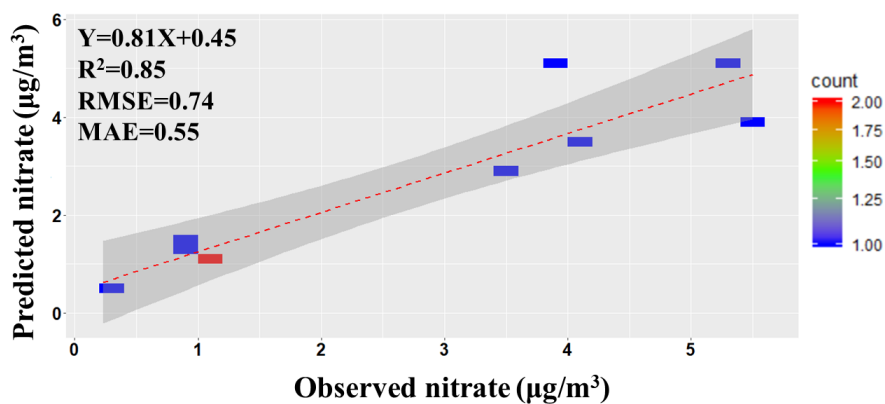
747 **Fig. 3** Density scatterplots of 10-fold cross-validation results for monthly  $\text{NO}_3^-$  estimation (Unit:  
748  $\mu\text{g}/\text{m}^3$ ) across China for the ensemble decision trees model including (a), RF (b), GBDT (c), and  
749 XGBoost (d), respectively.



750



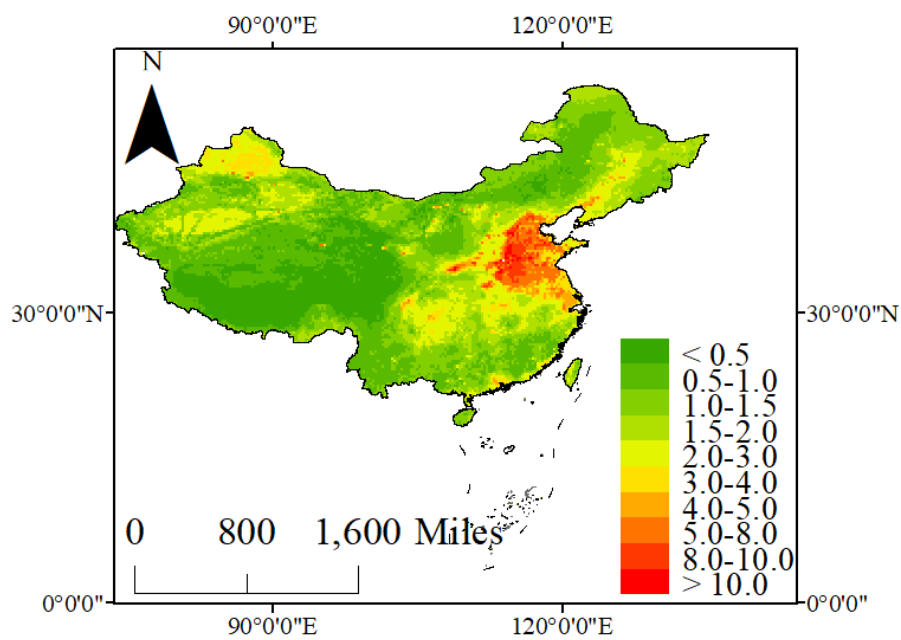
751 **Fig. 4** The transferability validation of the ensemble model in estimating  $\text{NO}_3^-$  concentration over  
752 China based on the unlearning observation data (Shen et al., 2013; Shen et al., 2009; Wang et al.,  
753 2019a; Xu et al., 2018b). The linear regression curve is added in the figure. The blue square  
754 represents the data points, and the red dashed line denotes the best-fit line through the data points.



755



756 **Fig. 5** The spatial pattern of ambient  $\text{NO}_3^-$  concentration ( $\mu\text{g}/\text{m}^3$ ) over China during 2005-2015.

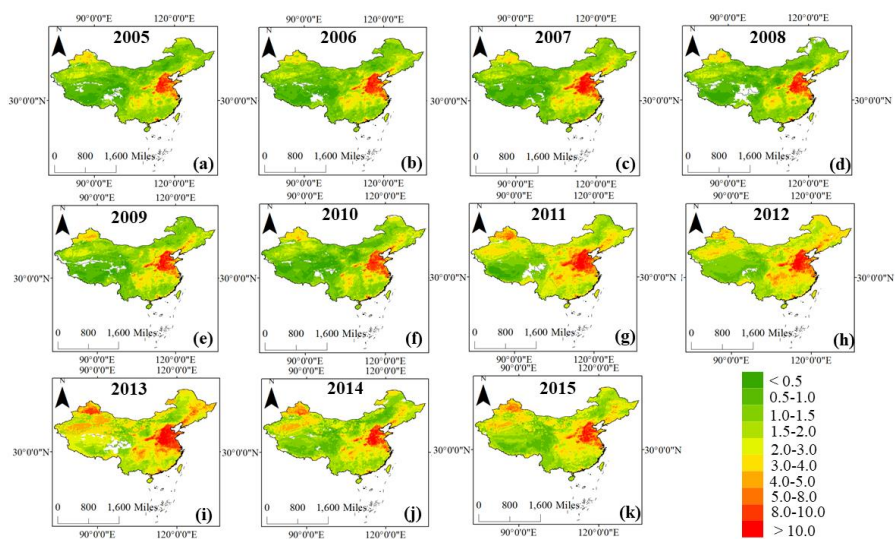


757





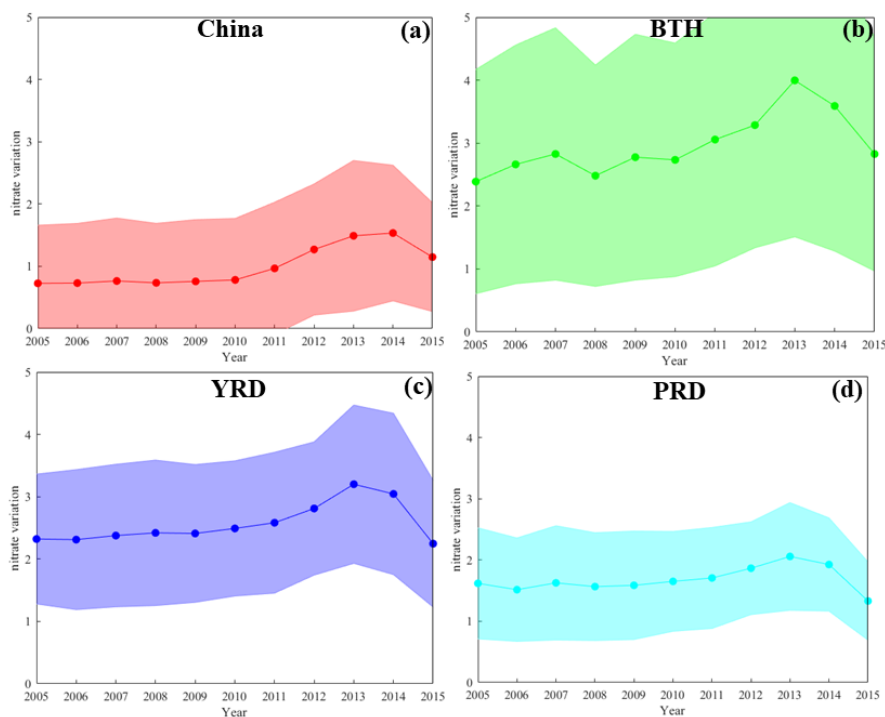
758 **Fig. 6** Satellite-derived annual mean  $\text{NO}_3^-$  concentration ( $\mu\text{g}/\text{m}^3$ ) across the entire China from (a)-  
759 (k) 2005-2015.



760



761 **Fig. 7** The annual mean  $\text{NO}_3^-$  concentrations in major regions across China during 2005-2015. The  
762 solid lines denote the mean  $\text{NO}_3^-$  concentrations and the shadow represents the range of  $\text{NO}_3^-$   
763 concentrations.

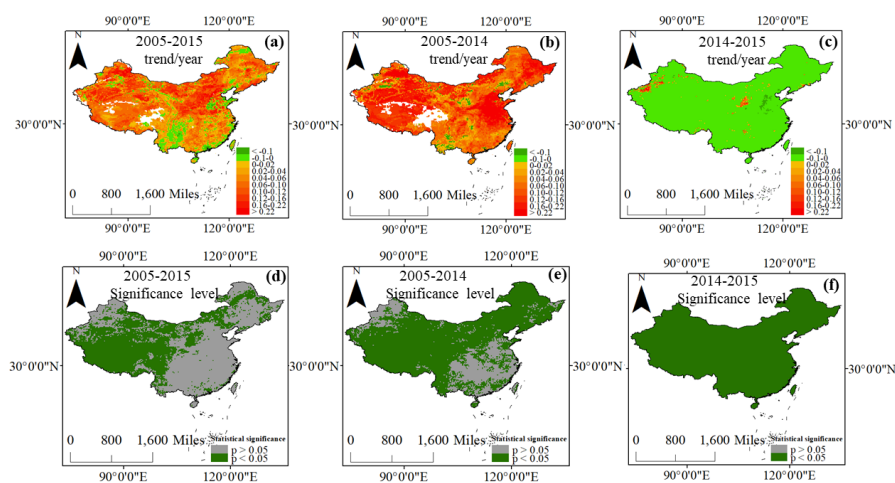


764

765



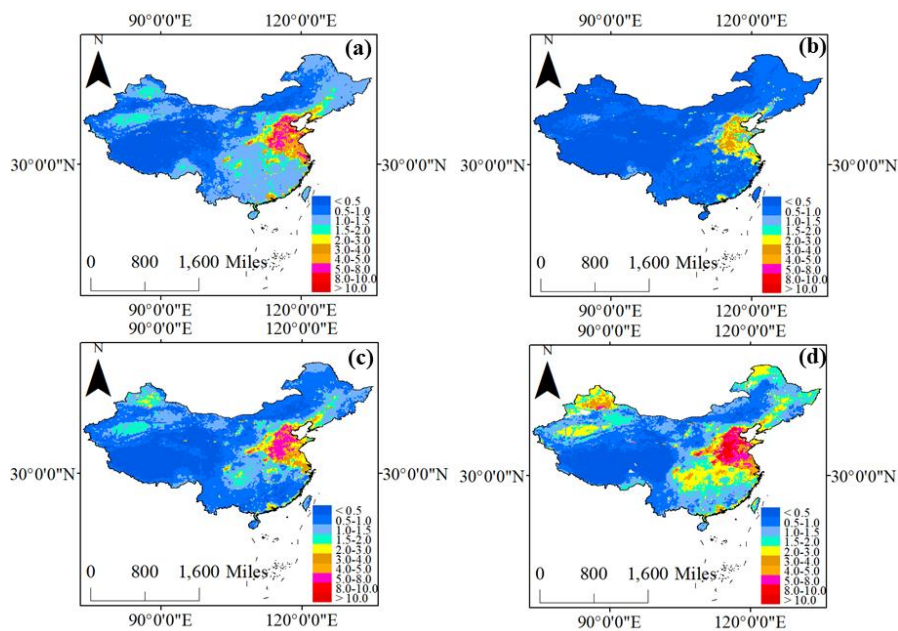
766 **Fig. 8** The long-term trends of  $\text{NO}_3^-$  concentrations and significance levels in China (a, b, and c  
767 denote the annual variation of ambient  $\text{NO}_3^-$  concentration during 2005-2015, 2005-2014, and 2014-  
768 2015, respectively. d, e, and f represent the significance level of  $\text{NO}_3^-$  trend during these periods).  
769 The pale green color denotes the regions with the significant variation of ambient  $\text{NO}_3^-$   
770 concentrations ( $p < 0.05$ ), while the gray color represents the regions with insignificant variation of  
771  $\text{NO}_3^-$  concentrations.



772



773 **Fig. 9** The mean concentrations of ambient  $\text{NO}_3^-$  in spring (a), summer (b), autumn (c), and winter  
774 (d) during 2005-2015 over China, respectively.



775



776 **Table 1** The cross-validation result of  $\text{NO}_3^-$  estimation over China during 2010-2015.

Season	R <sup>2</sup> value	Slope	RMSE ( $\mu\text{g}/\text{m}^3$ )	MAE ( $\mu\text{g}/\text{m}^3$ )
2010	0.62	0.60	1.39	0.90
2011	0.88	0.85	0.32	0.24
2012	0.89	0.86	0.33	0.28
2013	0.83	0.82	0.64	0.43
2014	0.74	0.76	1.50	1.04
2015	0.78	0.78	1.35	0.86

777



778 **Table 2** The cross-validation result of  $\text{NO}_3^-$  estimation over China in four seasons.

Season	R <sup>2</sup> value	Slope	RMSE ( $\mu\text{g}/\text{m}^3$ )	MAE ( $\mu\text{g}/\text{m}^3$ )
Spring	0.80	0.80	0.71	0.48
Summer	0.85	0.84	0.29	0.20
Autumn	0.80	0.78	1.10	0.70
Winter	0.75	0.73	1.85	1.23

779



780 **Table 3** The cross-validation result of  $\text{NO}_3^-$  estimation over China in different regions (Northeast  
781 China includes Heilongjiang, Jilin, and Liaoning provinces; NCP includes Beijing, Tianjin, Hebei,  
782 Henan, Shandong, and Shanxi provinces; Southeast China includes Jiangsu, Zhejiang, Fujian,  
783 Guangdong, Jiangxi, Anhui, Hunan, Hainan, Shanghai, and Hubei provinces; Southwest China  
784 includes Yunnan, Guangxi, Sichuan, Tibet, Chongqing, and Guizhou provinces; Northwest China  
785 includes Inner Mongolia, Xinjiang, Gansu, Qinghai, Ningxia, and Shaanxi.

Season	R <sup>2</sup> value	Slope	RMSE ( $\mu\text{g}/\text{m}^3$ )	MAE ( $\mu\text{g}/\text{m}^3$ )
Northeast China	0.44	0.43	1.30	0.81
NCP	0.70	0.64	1.74	1.06
Southeast China	0.59	0.57	1.50	0.84
Southwest China	0.60	0.59	2.08	1.41
Northwest China	0.58	0.52	2.06	1.38

786



787 **Table 4** The trend analysis of  $\text{NO}_3^-$  concentrations in China, BTH, YRD, and PRD regions during  
788 2005-2015.

Period	Trend	China	BTH	YRD	PRD
2005-2014	Trend ( $\mu\text{g}/\text{m}^3/\text{year}$ )	0.08	0.13	0.08	0.03
	Significance	$p < 0.05$	$p < 0.05$	$p < 0.05$	$p < 0.05$
2014-2015	Trend ( $\mu\text{g}/\text{m}^3/\text{year}$ )	-0.40	-0.76	-0.79	-0.59
	Significance	$p < 0.05$	$p < 0.05$	$p < 0.05$	$p < 0.05$
2005-2015	Trend ( $\mu\text{g}/\text{m}^3/\text{year}$ )	0.04	0.04	-0.01	-0.03
	Significance	$p < 0.05$	$p > 0.05$	$p > 0.05$	$p < 0.05$

789